5-1-2012

Synthesis and High-Pressure Structural Studies of AuX2 (X= Al, Ga, In) Compounds

Jason Lee Baker
University of Nevada, Las Vegas, futuredrjasonbaker@gmail.com

SYNTHESIS AND HIGH-PRESSURE STRUCTURAL STUDIES OF AUX_2 (X = AL, GA, IN) COMPOUNDS

By

Jason L. Baker

Bachelor of Science in Physics
University of Nevada, Las Vegas
2008

A thesis submitted in partial fulfillment
of the requirements for the

Master of Science Degree in Physics

Department of Physics and Astronomy
College of Sciences
The Graduate College

University of Nevada, Las Vegas
May 2012

THE GRADUATE COLLEGE

We recommend the thesis prepared under our supervision by

Jason L. Baker

entitled

Synthesis and High-Pressure Structural Studies of AUX_2 (X=AL, GA, IN) Compounds

be accepted in partial fulfillment of the requirements for the degree of

Master of Science in Physics
Department of Physics and Astronomy

Andrew Cornelius, Committee Chair

Michael Pravica, Committee Member

Changfeng Chen, Committee Member

Ravhi Kumar, Committee Member

Clemens Heske, Graduate College Representative

Ronald Smith, Ph. D., Vice President for Research and Graduate Studies
and Dean of the Graduate College

May 2012

ABSTRACT

SYNTHESIS AND HIGH-PRESSURE STRUCTURAL STUDIES OF AUX_2 (X = AL, GA, IN) COMPOUNDS

by

Jason Baker

Dr. Andrew Cornelius, Defense Committee Chair and
Dr. Ravhi Kumar, Defense Committee Co-Chair
University of Nevada, Las Vegas

Three intermetallic compounds, AuX_2 (X = Al, Ga, In), were synthesized by arc-melting proper stoichiometric ratios of high purity Au, Al, Ga, and In. They were found to be single-phase in the CaF_2 type *Fm3m* crystalline structure. Interest in these particular intermetallic materials is due to intriguing pressure-induced behavior such as electronic topological transitions (ETTs), and structural phase transitions as well as their use in a variety of practical applications such as a solar spectral absorber and in electronic circuitry. In this study, the high-pressure structure of these materials was studied using high resolution synchrotron x-ray diffraction (XRD) at the Advanced Photon Source at Argonne National Laboratory. Pressure induced structural transitions were observed below 20 GPa in all the samples and the equation of state (EOS) was determined for the *Fm3m* phase. Our experiments show that compressibility of these compounds vary greatly, where $AuIn_2$ is the most compressible and $AuAl_2$ is the least compressible. Effect of hydrostaticity on the structural phase transition and the phase transition sequence are discussed.

ACKNOWLEDGMENTS

I would like to thank the following people:

Dr. Andrew Cornelius for allowing me to work in this lab and especially for his patience over the many years.

Dr. Ravhi Kumar for the opportunities for collaboration, sharing his knowledge of DACs, and always finding time to answer my endless questions.

Dr. Clay Crow for use of his XRD machine.

Argonne National Laboratories, and the HPCAT Sector 16 beam-line scientists for their endless help with experiments.

And my family and friends for all the support.

TABLE OF CONTENTS

LIST OF TABLES

LIST OF FIGURES

Chapter 1: Introduction

Intermetallic compounds encompass a vast range of materials with applications ranging from brass, an alloy of Cu and Zn, first used in ancient times to fabricate weapons and pottery, to superconductors such as Nb_3Sn with a critical temperature of 13 K, to uses in diesel engine turbocharger rotors and hydroturbines with compounds such as Ni_3Al and $NiAl_3$ [1, 2]. Insight into the basic properties of such materials is important as it brings the potential to better understand existing compounds and applications as well as find new compounds and applications. One of the most fundamental of these basic properties is the crystal structure, or how the atoms are arranged in the smallest repeated building block for the material. When these compounds are exposed to extreme conditions, such as high pressure, temperature, magnetic field, etc., the crystal structure as well as other physical and chemical properties of the material has the potential to change. Understanding these changes under extreme conditions is vital to furthering the knowledge of materials and applications.

In this study, the effects of pressure on the crystal structure of a group of intermetallic compounds were examined. The group chosen for this thesis is AuX_2 where X = Al, Ga, and In. These intermetallics crystallize in the CaF_2 structure and have been of significant interest due to their properties and applications. $AuAl_2$ has good electrical conductivity and as such is used as a spectral selective solar absorber [3]. It is also a type - I superconductor, along with $AuIn_2$, with their superconducting transition temperatures being 207 and 160 mK, respectively [4]. In addition, nuclear ferromagnetism and superconductivity were found to co-exist in $AuIn_2$ [5]. The material $AuGa_2$ has been reported to have useful properties in electronic circuitry [6]. Also of importance is that

the AuX_2 intermetallic alloys undergo electronic topological and structural transitions under pressure. [7]

Due to the various applications and interesting properties of these materials, the crystal structure properties of the AuX_2 compounds are important both at room temperature and high P-T conditions. In this thesis, the state of the art high resolution synchrotron high-pressure x-ray diffraction (HP-XRD) technique has been used to determine how the crystal structure of these compounds change with increasing pressure. The title compounds were prepared in single phase in our laboratory and were characterized. The samples were then subjected to high pressures with Merrill-Bassett type diamond-anvil cells (DACs), which allowed pressure of maximally 25 GPa to be reached, and for each pressure reached in the DACs, XRD patterns were obtained which contain information directly related to the crystal structure of the materials.

Chapter 2: Background

This section will give an overview of the literature existing on the compounds being studied in this thesis. Direct comparison to the data collected in the experiments done for this study will be discussed in the Results/Discussion section as well as additional details related to the literature experiments and theoretical calculations.

$AuAl_2$

In 2005, Garg *et al.* studied $AuAl_2$ using HP-XRD techniques. The authors found that $AuAl_2$ undergoes a phase transition beginning around 13 GPa and fully transforms at 17 GPa. According to their findings, the sample did not show any signs of structural transition until 13 GPa and they were able to obtain an experimental equation of state (EOS) up to 17 GPa [8].

With regards to the high-pressure phase of $AuAl_2$, the authors were able to index the high pressure phase to a general orthorhombic structure, but were unable to fully index this phase due to a small number of peaks. They did narrow the possibilities to four orthorhombic structures from systematic absences observed. These four possibilities are *$Pnm2_1$*(31), *Pnmm*(59), *$Pn2_1$*(33), and *Pnma*(62) [8].

The high-pressure XRD data for $AuAl_2$ was also examined for evidence of an electronic topological transition (ETT). They calculated the universal EOS (UEOS) and subsequently determined that $AuAl_2$ did not undergo an ETT [8].

In 2007, Verma *et al*. determined the high-pressure structural phase of $AuAl_2$ using first-principle calculations. Their theoretical results predict a structural phase transition at 18.7 GPa to a primitive orthorhombic structure (*Pnma*) [9].

$AuGa_2$

Using HP-XRD techniques, $AuGa_2$ was studied, and it was determined that it underwent a pressure-induced structural phase transition near 7 GPa by Garg *et al.* in 2006. Up to 7 GPa, the structure of $AuGa_2$ was found to have the expected CaF_2 structure. The high-pressure phase was indexed to a low-symmetry orthorhombic phase closely related to the original cubic phase, but this was only in the range 7 – 10 GPa. After 10 GPa, the diffraction peaks were reported to change intensity continuously making it difficult to index the patterns in this region. An experimental EOS was determined up to 7 GPa [10].

As with $AuAl_2$, this sample was also examined for an ETT by the authors. For $AuGa_2$, it was determined from the UEOS that definite evidence for a possible ETT existed at 3.2 GPa [10].

$AuIn_2$

This sample was examined using high-pressure XRD by Godwal *et al.* in 1998. From this data, the authors reported evidence of a pressure-induced structural transition after 8 GPa and this new phase is stable until 15 GPa. It was indexed to a monoclinic cell $P2_1/c$. In this 1998 study, the UEOS was also calculated and a deviation from linearity was reported in the UEOS plot. From this, the authors concluded there was evidence of a possible ETT between 2 – 4 GPa [11].

In 2002, Godwal *et al.* reaffirms the presence of a structural phase transition beyond 9 GPa in $AuIn_2$. The XRD patterns below 9 GPa were indexed to the ambient *Fm3m* structure and the patterns after 9 GPa were determined to be of a different phase.

An UEOS was calculated in the paper and provided more evidence of a possible ETT around 3.6 GPa [12].

In a 2008 paper, Godwal *et al*. again performs HP-XRD measurements on $AuIn_2$ and find no evidence of the previously reported phase transition at 9 GPa. $AuIn_2$ is reported to retain the CaF_2 structure until 24 GPa, where it then becomes amorphous. In the region of 20 – 24 GPa, the sample is suggested to be metastable and that the structural transitions in this material may be sensitive to non-hydrostatic conditions present in the DAC [13].

Density Functional Theory Calculations

There have also been studies done using density functional theory (DFT) calculations to determine the onset pressure of electronic topological and structural phase transitions as well as obtain parameters such as ambient unit cell volume, bulk modulus, and the derivative of the bulk modulus for all three samples. Li *et al* determined that electronic topological transitions were present in $AuIn_2$ and $AuGa_2$, but not $AuAl_2$ which agrees with the experimental results seen in the literature [7]. Also, several DFT methods were utilized which allowed them to calculate and compare the parameters just mentioned to those found in the experimental literature [7]. When these parameters are compared with the experimental values, some of the DFT methods overestimate the bulk modulus and its derivative, but most of the comparisons between theoretical and experimental results in the literature tend to agree fairly well.

General Theory

This section will provide some basic theoretical framework for the experimental methods and analysis to be used in the rest of the thesis. Ruby fluorescence, x-ray diffraction, and the Birch-Murnaghan equation of state will be discussed.

Ruby Fluorescence

Ruby, $Al_2O_3 : Cr^{3+}$, is a widely used pressure sensor in DAC experiments. When photons are incident on the Al_2O_3 with Cr^{3+} doping, the electrons in the ground state of Cr^{3+} are raised to short-lived excited states (E_3 and E_4 in **Fig. 1**) and immediately fall to a longer lived meta-stable state (E_2 in **Fig. 1**). The decay from the short-lived energy states to the meta-stable long-lived state is a non-radiative transition, which means no photons are released due to this transition. E_2 is split into two energy levels due to spin splitting and both of these levels are long-lived meta-stable states. When the electrons in E_3 and E_4 transition into these two lower energy states, they will then eventually fall from the split E_2 states to the ground state releasing a photon. The photon released due to the higher of these two E_2 states corresponds to the R_1 ruby spectrum line and the lower of the two corresponds to the R_2 ruby spectrum line. This process is illustrated in **Fig. 1**.

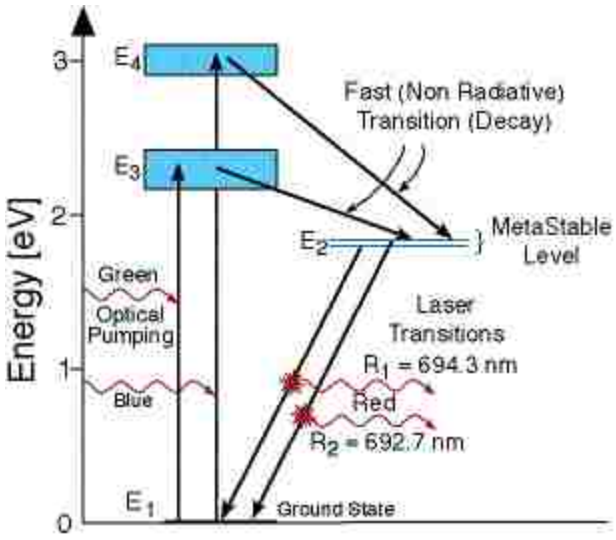

Figure 1. Energy Level Diagram for Fluorescence of Ruby [14]

When pressure is applied to the ruby, the energy difference between the two E_2 states and the ground state changes in a well-studied manner. If the ruby is made to fluoresce, the wavelength of this light can be measured, and from this, the pressure being applied to the ruby can be determined. A typical ruby fluorescence spectrum is shown in **Fig. 2**, where a spectrum is given for both ambient pressure and 10 GPa. As stated, the spectra will shift when pressure is applied to the ruby which is clearly seen by change in the wavelength between the two different pressures. The R_1-line is at the higher wavelength and R_2-line at the lower wavelength for both spectra.

The R_1-line is the ruby spectrum line typically used in order to measure the pressure. In 1977, Mao, *et al*. developed an equation to calculate the pressure, ***P***, by knowing the shift of the R_1-line from its ambient value [16]. This relationship is given:

$$P(\text{GPa}) = 380.8\left[\left((\lambda/694.2)\right)^5 - 1\right]. \qquad \text{Equation 1}$$

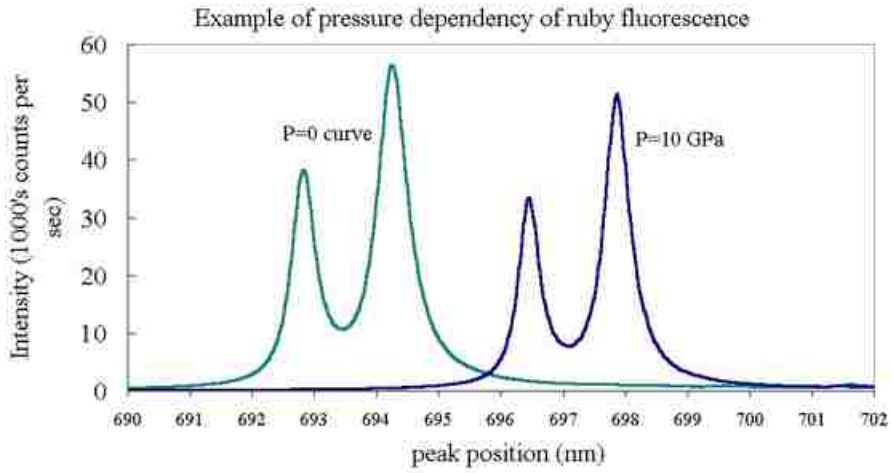

Figure 2. Typical Ruby Fluorescence Spectra for Ambient Pressure and 10 GPa [15]

In this equation, λ is the peak position of the R_1-line from in nanometers. When λ is equal to 694.2 nm, it is easily seen from Eq. 1 that the pressure will be zero. In **Fig. 2**, the ruby spectrum corresponding to 10 GPa has its R_1-line at approximately 698 nm and if this is inserted into **Eq. 1** it will give 10.5 GPa.

The ruby fluorescence spectrum also gives information about how hydrostatic the conditions are in the DAC. Depending on the pressure-transmitting medium used for a particular experiment, the peaks in the ruby fluorescence spectrum will broaden at different pressures. For pressure-transmitting media such as 4:1 Methanol:Ethanol, this broadening of the peaks occurs around 10 GPa. This is important because a quantitative measure of the hydrostatic conditions inside the DAC can be obtained through measuring the width of the spectrum lines.

Crystal Structure

The crystal structure of a material can be described mathematically by a lattice, which is a repeated set of mathematical points in a particular arrangement. Each of these points in the lattice can have a group of atoms attached to it, referred to as a basis. In the ideal case, a crystal consists of an infinite repetition of these basis attached to the lattice. The lattice is mathematically defined by three translation vectors $\mathbf{a_1}$, $\mathbf{a_2}$, and $\mathbf{a_3}$ in such a way that the crystal looks the same when viewed from the point **r** as when viewed from any other point translated by an integral multiple of the translation vectors. **Eq. 2** gives the mathematical representation of this statement where **r'** is the point translated to from the original point **r** and $\mathbf{u_1}$, $\mathbf{u_2}$, and $\mathbf{u_3}$ are integers.

$$\boldsymbol{r'} = \boldsymbol{r} + u_1\boldsymbol{a_1} + u_2\boldsymbol{a_2} + u_3\boldsymbol{a_3} \qquad \text{Equation 2}$$

It is this periodicity of the lattice that gives rise to many physical properties of the material and is a significant reason why a fundamental understanding of the crystal structure of materials is integral to explaining other physical properties [17].

These lattices, forming the building blocks of crystalline solids, can be categorized by their symmetries and their arrangement of lattice points. The most general lattice is the triclinic lattice where no sides and no angles are equal to each other, thus it has the least amount of symmetry out of all the lattices. There are 13 special lattices which are grouped into systems according to seven types of cells. The seven systems are listed in **Table 1** along with the particular number of lattices contained in each system as well as the restrictions on the cell axes and angles that define the particular system. An example of the different lattices contained in a particular system can be seen with cubic,

which has three lattices in its system. These lattices are simple cubic, base-centered cubic, and face-centered cubic.

System	Number of Lattices	Restrictions on conventional cell axes and angles
Triclinic	1	$a_1 \neq a_2 \neq a_3$ and $\alpha \neq \beta \neq \gamma$
Monoclinic	2	$a_1 \neq a_2 \neq a_3$ and $\alpha = \gamma = 90° \neq \beta$
Orthorhombic	4	$a_1 \neq a_2 \neq a_3$ and $\alpha = \gamma = \beta = 90°$
Tetragonal	2	$a_1 = a_2 \neq a_3$ and $\alpha = \gamma = \beta = 90°$
Cubic	3	$a_1 = a_2 = a_3$ and $\alpha = \gamma = \beta = 90°$
Trigonal	1	$a_1 = a_2 = a_3$ and $\alpha = \beta = \gamma < 120°$
Hexagonal	1	$a_1 = a_2 \neq a_3$, $\alpha = \beta = 90°$ and $\gamma = 120°$

Table 1. All 14 possible lattice types in three dimensions [17].

X-Ray Diffraction

XRD is a technique using the diffraction of x-rays off the lattice planes of materials, or more specifically through interaction with the electron distribution around the atoms, in order to gather information about the crystal structure. With this technique, information about the unit cell comprising a material can be determined, such as the lattice parameters (or distance between lattice planes) which can be used to calculate the volume of the unit cell. There are two main types of XRD used, those being powder XRD and single-crystal XRD. The technique discussed here and used for these experiments is powder XRD.

An ideal powder sample consists of a very large number of randomly oriented single-crystals. If x-ray photons are incident on a crystal, then each of the parallel planes of the atoms in the crystal lattice will specularly reflect a small fraction of the radiation.

When the reflections constructively interfere, the diffracted beams are strongest. Bragg's Law gives the conditions that must be met in order to have this constructive interference and thus, diffraction peaks. This equation is given as **Eq. 3**, and its derivation, however simple, is given elsewhere. Also, to aid with the visualization of the geometry of the incident x-ray photons and the lattice planes, Fig. 3 shows this geometry in some detail.

$$2\,d\sin\theta = n\,\lambda \qquad \text{Equation 3}$$

In this equation**, λ** represents the wavelength of the incident x-ray photons, **θ** represents the angle at which the incident photon diffracts off the lattice planes where the distance between these lattice planes is given by **d** in the equation. [17]

Using this relationship, both angle-dispersive and energy-dispersive XRD can be conducted. Energy-dispersive XRD is not used in this study, but it is when the angle is held constant while the wavelength of the incident x-ray photons is scanned. Angle-dispersive XRD, the method used in this thesis, is when the wavelength of the incident x-ray photons is left unchanged and instead the angle at which the incident photons strike the lattice planes is changed. This can be done by rotating the sample itself, moving the detector through a large angle around the sample, or using the premise of powder diffraction as stated earlier.

Since the wavelength is held constant and **θ** is variable when using angle-dispersive XRD, Bragg's Law can be rearranged to obtain $\boldsymbol{\sin\theta = \frac{n\,\lambda}{2\,d}}$. This rearranged equation reveals that for a particular lattice spacing, there is a particular angle that will satisfy this equation. At this angle, the reflections constructively interfere to create a peak in the intensity of collected photons when measured as a function of the angle.

Equation of State (Birch-Murnaghan)

The EOS is a mathematical equation whose variables are state functions such as pressure, volume, temperature, or internal energy and describes the state of matter under a variety of physical conditions. For gaseous materials, the ideal gas law, van der Waals' EOS, and other theoretically and experimentally derived EOS's exist to describe the behavior of gaseous molecules in different physical conditions. For solid materials, there also exist a variety of EOS's capable of describing the behavior of solid materials for various physical environments such as the Birch-Murnaghan, Mie-Gruneisen, Rose-Vinet, and other EOS's. For this thesis, the Birch-Murnaghan EOS will be used as it is used in almost all literature regarding the studying of materials at high pressure. [18]

$$P(V) = \frac{3B_0}{2}\left[\left(\frac{V_0}{V}\right)^{\frac{7}{3}} - \left(\frac{V_0}{V}\right)^{\frac{5}{3}}\right]\left\{1 + \frac{3}{4}(\mathrm{B'}_0 - 4)\left[\left(\frac{V_0}{V}\right)^{\frac{2}{3}} - 1\right]\right\} \quad \text{Equation 4}$$

Equation 4 gives the Birch-Murnaghan EOS. This equation gives the pressure as a function of the unit cell volume at a constant temperature. In this equation, the fit parameters are $\mathbf{B_0}$ which is the initial bulk modulus, $\mathbf{V_0}$ which is the initial unit cell volume, and $\mathbf{B'_0}$ is the first pressure derivative of the bulk modulus. **V** is the unit cell volume as measured in the experiment being performed and **P(V)** is the pressure being applied to the sample corresponding to the particular **V**. The bulk modulus is inversely proportional to the compressibility and as such, the bulk modulus can be used as a measure of the compressibility of materials.

Experimental Details

This section will discuss sample synthesis, characterization of the samples, details of the high-pressure x-ray diffraction techniques employed, and the methods of analysis used on the data collected.

Sample Synthesis

All three samples were prepared using high purity (99.99%+) Au, Ga, and In purchased from Sigma Aldrich. Appropriate stoichiometric ratios of the components for each compound were weighed and mixed thoroughly together using a mortar and pestle. A pellet of each of the three samples was made using a 7mm pellet dye and a hydraulic press to provide pressures of 3000 - 4000 psi. Each of the pellets was then arc-melted in an argon atmosphere in the UNLV Physics department's arc-melting furnace, which is shown in **Fig 3**.

Figure 3. Arc-melting furnace and copper hearth.

This device consists of a copper hearth where the sample is placed, a tungsten rod to apply the current, a rotary-vane vacuum pump, and a tank of high-purity argon gas. The hearth is inserted at the bottom of the chamber. With the hearth in place, the chamber is repeatedly evacuated to 30mmHg and filled to 15mmHg with argon several times to

ensure all contaminants are flushed out of the chamber. After this process, the chamber is again evacuated and then filled with argon to 15 mmHg.

Tapping the tungsten rod to the side of the copper hearth will create a closed circuit between the rod and hearth, thus producing a high-temperature arc from the tip of the rod to the copper. This arc is then positioned over the sample and a reaction takes place. Since the sample is a pellet having two sides, it must be flipped and reacted in the same fashion on the opposite side as well to ensure an evenly reacted ingot. This was done for all three samples.

After each of the samples was reacted, the ingots resulting from the arc-melting were lightly grinded with fine sand-paper to remove any surface contamination. Acetone and methanol were used to ensure the surface was clean after grinding it with the sand-paper. The ingots were then broken into small pieces, which were ground into a fine powder using a mortar and pestle.

Sample Characterization

After this process, each of the samples were taken to the XRD facilities at UNLV. An X-Pert XRD apparatus with a x-ray wavelength of 1.54 Å (Cu Kα) was used. The powdered samples were placed on a silicon wafer, which has a minimal background contribution, and XRD data was collected over the two-theta range of 5° to 85° for each of the samples. In order to compare the XRD patterns collected for the samples in this thesis to the samples in literature, reference XRD patterns were calculated using PowderCell software by using the cell parameters stated in the literature on each of the compounds. The XRD patterns as obtained from the GeoScience's facility are shown in

Fig. 4 as well as the calculated reference patterns. The red XRD pattern in the plots correspond to the reference data, and the black XRD pattern in the plots is the data collected for this experiment. As evidenced by the graphs, the reference XRD patterns and the patterns collected for this experiment agree fairly well for each of the compounds.

Using Materials Data Incorporated (MDI) Jade 7.1 software [19], the XRD patterns from this experiment can be indexed to the CaF_2 phase with lattice parameters in good agreement with literature values. Only a few very small peaks not corresponding to the CaF_2 phase show up in the XRD patterns, but due to the fact that they are quite small, they are not significant.

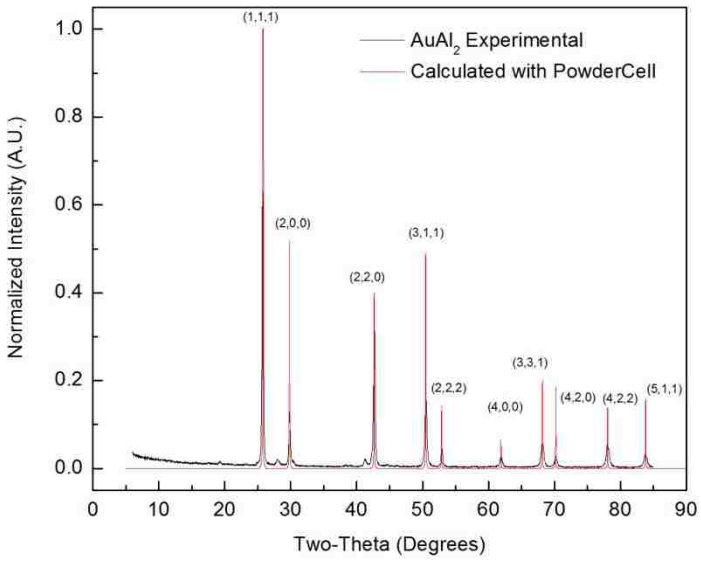

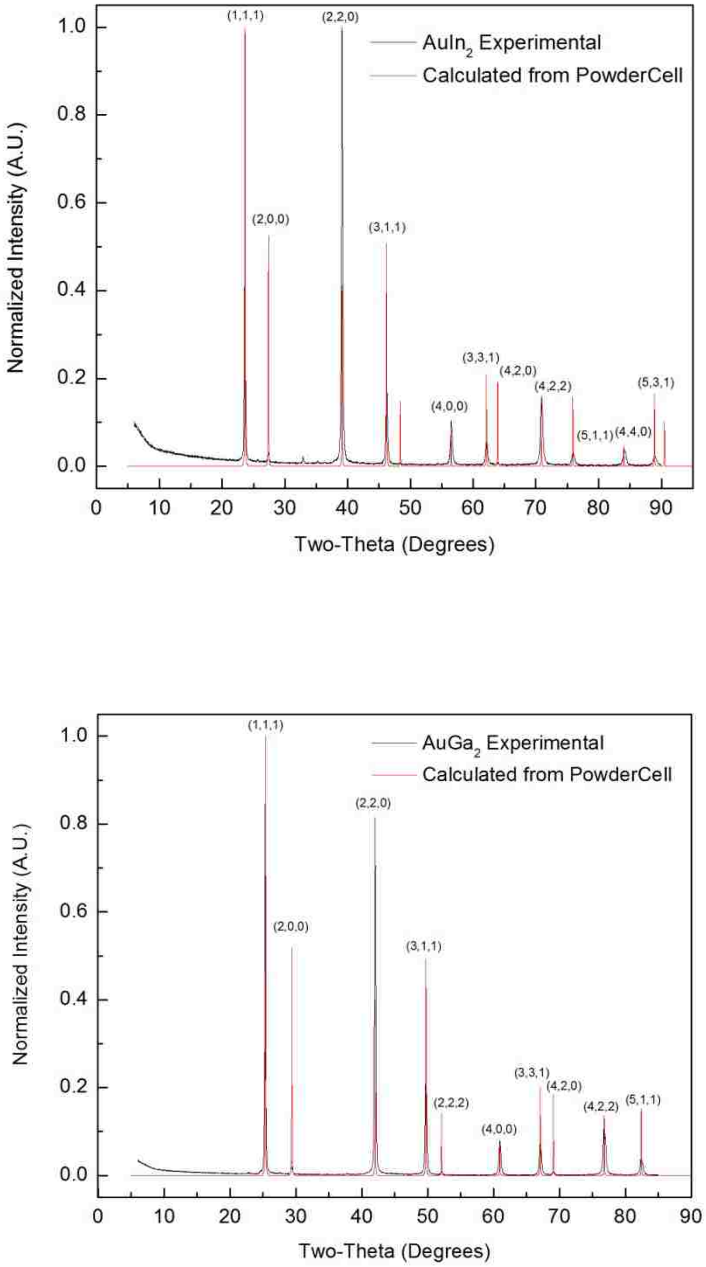

Fig 4. Calculated and collected XRD patterns for $AuAl_2$, $AuIn_2$, and $AuGa_2$

For each of the XRD patterns corresponding to the samples studied in this thesis, MDI Jade software was used to obtain the lattice parameter, **a**. The values for these samples and corresponding literature values can be found in **Table 2** for comparison.

	Literature (Å)	Observed (Å)
$AuAl_2$	6.005	5.993 ± 0.001
$AuIn_2$	6.517	6.507 ± 0.001
$AuGa_2$	6.079	6.069 ± 0.002

Table 2. Lattice parameter comparison between literature and this experiment

The errors listed for the observed data are obtained from fitting the XRD peaks to the CaF_2 structure for each of the samples using MDI Jade. These error bars do not take into account any instrumental effects or differences occurring due to sample preparation. The literature values did not have errors listed. Although the values do not agree within the error bars presented, due to fact they are not including anything besides statistical fluctuations of the data from the fit, there may be small systematic effects causing the difference.

High-Pressure XRD

Multiple experimental runs of measurements have been taken on these samples. All sets of measurements were taken in a Merrill-Bassett type DAC. A photograph of a Merrill-Bassett type DAC is shown in **Fig. 5**. This DAC consists of two stainless steel triangular shaped pieces where one has a beryllium backing plate and one has a tungsten carbide backing plate. The diamonds are secured onto these backing plates with a steel collar that is screwed into the backing plate. Once the diamonds are secured to the backing plates, they must be aligned with respect to each other. Three small set screws are used to align the diamonds with each other.

Figure 5. Merrill-Bassett type DAC

For each set of measurements, the diamonds were carefully aligned for each DAC. Stainless steel gaskets were used for all the measurements and had an initial thickness of **250 µm**. They were then pre-indented after the diamonds had been aligned. This pre-indentation is done by placing the gasket between the diamonds of the DAC, secured by a steel gasket holder screwed into the backing plate, and pressurizing until the gasket material has formed to the shape of the diamonds and is **50 - 60 µm** in thickness at the culet face. A hole in the center of each of the gaskets was then drilled, using electric discharge machining (EDM). The size of the hole differed depending on the size of the diamond culet's diameter. The culet diameter for the different experimental runs was **300 µm**, **400 µm**, and **500 µm**. The hole drilled in the center of the gaskets was **100**, **130**, and **160 µm**, respectively for the different culet diameters.

With the gaskets pre-indented and holes drilled, the gaskets were again secured with the gasket holder on top of each of the diamonds, and the sample and ruby sphere were placed into the hole. Then, the pressure-transmitting medium was put in as well. A 4:1 Methanol:Ethanol mixture was used as the pressure-transmitting medium (PTM) for all of the measurements and was inserted by use of a syringe. The DACs were

immediately closed and slight pressure was given by tightening the screws to ensure the PTM, sample, and ruby sphere were trapped in the hole (or sample chamber). A 405 nm laser is shined into the sample chamber and a spectrometer is used to collect fluorescence spectra from the ruby sphere in order to determine the starting pressure. Using the Mao ruby scale [15], the pressure was determined to be approximately 1 GPa for each sample.

The high-pressure XRD experiments were carried out at Sector 16 at the Advanced Photon Source (APS) at Argonne National Laboratory. All three of the samples were run on both the insertion device beam-line (ID-B) and the bending magnet beam-line (BM-D). Exposure times on ID-B were between 10 to 30 seconds throughout the extent of the experiments, and exposure times on BM-D were between 30 to 60 seconds.

The x-rays are directed into the DAC and diffract due to the sample inside. The diffracted photons travel out the conical side of the DAC and are collected on an image plate or CCD detector. The beam-line was initially calibrated using CeO_2 powder, for which the lattice spacing is well known. The wavelengths used throughout all the experiments on the samples are given in **Table 3**.

The pressure between each data collection was increased and determined by again shining a laser inside the DAC as mentioned previously to fluoresce the ruby sphere inside the sample chamber. Again using the Mao ruby scale [15], the pressure of the sample can be determined.

Experimental Run	Wavelength (Å)
1st	0.375710
2nd	0.407376
2nd	0.407351
2nd	0.407351
3rd	0.413364

Table 3. Wavelength values for the various experimental runs conducted

Analysis

The raw data files obtained from the XRD measurements are then read into FIT2D [20] along with the calibration values for each data set. An example of the raw MAR file before integration is shown in **Fig. 6**.

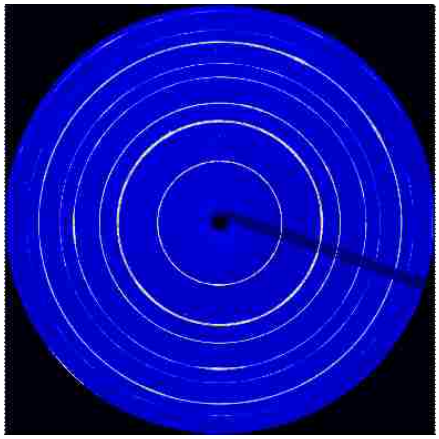

Figure 6. Example of raw MAR file before integration. ($AuIn_2$, 2.31 GPa)

Using these values, FIT2D integrates the raw data files and produces intensity versus two-theta plot datasets which can then be analyzed using MDI Jade software. This software was used to subtract the background from the data, index the peak positions to a library of crystal structures, and calculate and refine peak positions of the XRD patterns to a particular crystal structure, thus determining the lattice parameters of the sample.

With the crystal structure and lattice parameters known, a volume for the unit cell of the material can be calculated. This method of analysis was done for each pressure point, and with the unit cell volume at each pressure point known, the parameters in the Birch-Murnaghan EOS can be calculated. The parameters in the Birch-Murnaghan EOS were obtained by inputting the volume and pressure into a DOS run program built to fit this type of data to multiple EOS's including the Birch-Murnaghan EOS. With the parameters known for the Birch-Murnaghan EOS that fits best to the experimental data, a plot of the pressure and volume data with the Birch-Murnaghan EOS graphed as well can be created for each sample.

Results/Discussion

This section will be broken into two main parts. The first will present and discuss the results obtained from the XRD experiments performed for the low pressure phase of all three materials. The second part will present and discuss the results for the high pressure phases of these materials. The results will be compared to the literature and the differences and similarities will be illuminated and discussed.

Low Pressure Phase Results: $AuAl_2$

The evolution of the x-ray diffractions patterns for $AuAl_2$ is shown for one of the experimental runs performed up 26.4 GPa in **Fig. 7**. From **Fig. 7**, the similarities between the XRD patterns below 11 GPa are clearly observed by noticing the peaks remain unchanged except for a movement to higher angle values which corresponds directly with a decrease in lattice spacing and thus a decrease in unit cell volume. For the range of pressures of 1.68 GPa to 11.0 GPa, these XRD patterns can be indexed to the CaF_2 (Space Group *Fm3m*) as is observed at ambient pressures. For this discussion of the lower pressure phase of $AuAl_2$ the XRD patterns above 11.0 GPa will be ignored and discussed in a later section.

Using the analysis technique described earlier, the peak positions from these XRD patterns will give the lattice parameters and thus the volume of the unit cell for each pressure point. **Table 4** contains all the pressure and volume data including the volume error as determined from the peak position fitting in MDI Jade for $AuAl_2$ for all the experimental runs completed. A plot of the volume versus pressure is displayed in

Fig. 8. The fit parameters are listed in **Table 5** along with the values as found in the literature.

Pressure (GPa)	Volume ($Å^3$)	Error ($Å^3$)
0	215.38	
0.35	215.14	0.19
1.31	213.37	0.22
1.37	214.90	0.31
1.68	213.01	0.09
2.73	211.39	0.24
3.23	210.04	0.14
3.83	209.44	0.35
4.93	207.90	0.15
5.86	207.10	0.16
6.23	205.95	0.14
7.41	203.94	0.13
7.9	204.02	0.12
8.31	203.90	0.14
8.45	202.74	0.15
9.36	201.85	0.17
10.9	204.01	0.12
11.34	200.28	0.31

Table 4. Tabulation of pressure and volume data for $AuAl_2$ for three separate experimental runs

The Birch-Murnaghan EOS fit to the volume and pressure data can be compared to the literature by comparing the parameters found in **Table 5**. From the values in **Table 5**, it is evident that the bulk modulus, $\mathbf{B_0}$, as determined by this set of experiments is slightly higher than the experimental literature value. However, this higher result does agree fairly well with LDA experiment as this value is 126 GPa [8] as well as the FP-LAPW LDA result of 122 GPa [7]. This experiment's initial volume, V_0, is slightly lower than the experimental literature value as can be seen in the table, but does lie within the range of the theoretical results listed in the table. Lastly, the pressure derivative of the bulk modulus, $\mathbf{B_0'}$, was fixed at a value of four for both the experimental literature's and

this experiment's Birch-Murnaghan EOS fitting. The theoretically calculated values for $\mathbf{B_0'}$ are all slightly higher.

		V_0 (Å^3)	B_0 (GPa)	B_0'
$AuAl_2$	**Experiment**	215.7 (1)	122 (2)	4.0 (fixed)
	Literature (Experimental) [8]	216.5	111	4.0 (fixed)
	Literature (Theory) FP-LAPW [7]	LDA: 209.6 GGA: 217.1	LDA: 122 GGA: 108	LDA: 4.72 GGA: 4.81
	Literature (Theory) PP-PW [7]	LDA: 208.5 GGA: 220.3	LDA: 120 GGA: 103	LDA: 4.83 GGA: 4.49
$AuIn_2$	**Experiment**	275.5 (4)	68 (2)	9.0 (5)
	Literature (Experimental) [13]	276.8 (1)	62 (1)	9.5 (5)
	Literature (Theory) FP-LAPW [7]	LDA: 268.3 GGA: 295.4	LDA: 78 GGA: 62	LDA: 4.77 GGA: 4.11
	Literature (Theory) PP-PW [7]	LDA: 275.9 GGA: 286.2	LDA: 75 GGA: 58	LDA: 6.27 GGA: 5.77
$AuGa_2$	**Experiment**	224.0 (3)	90 (3)	4.0 (fixed)
	Literature (Experimental) [10]	224.6	98	4.0 (fixed)
	Literature (Theory) FP-LAPW [7]	LDA: 216.0 GGA: 236.0	LDA: 103 GGA: 68	LDA: 7.08 GGA: 6.28
	Literature (Theory) PP-PW [7]	LDA: 225.9 GGA: 233.7	LDA: 88 GGA: 73	LDA: 5.53 GGA: 5.09

Table 5. EOS fit parameters from our experiments and previously reported experimental results and theoretical results in the literature for all three samples

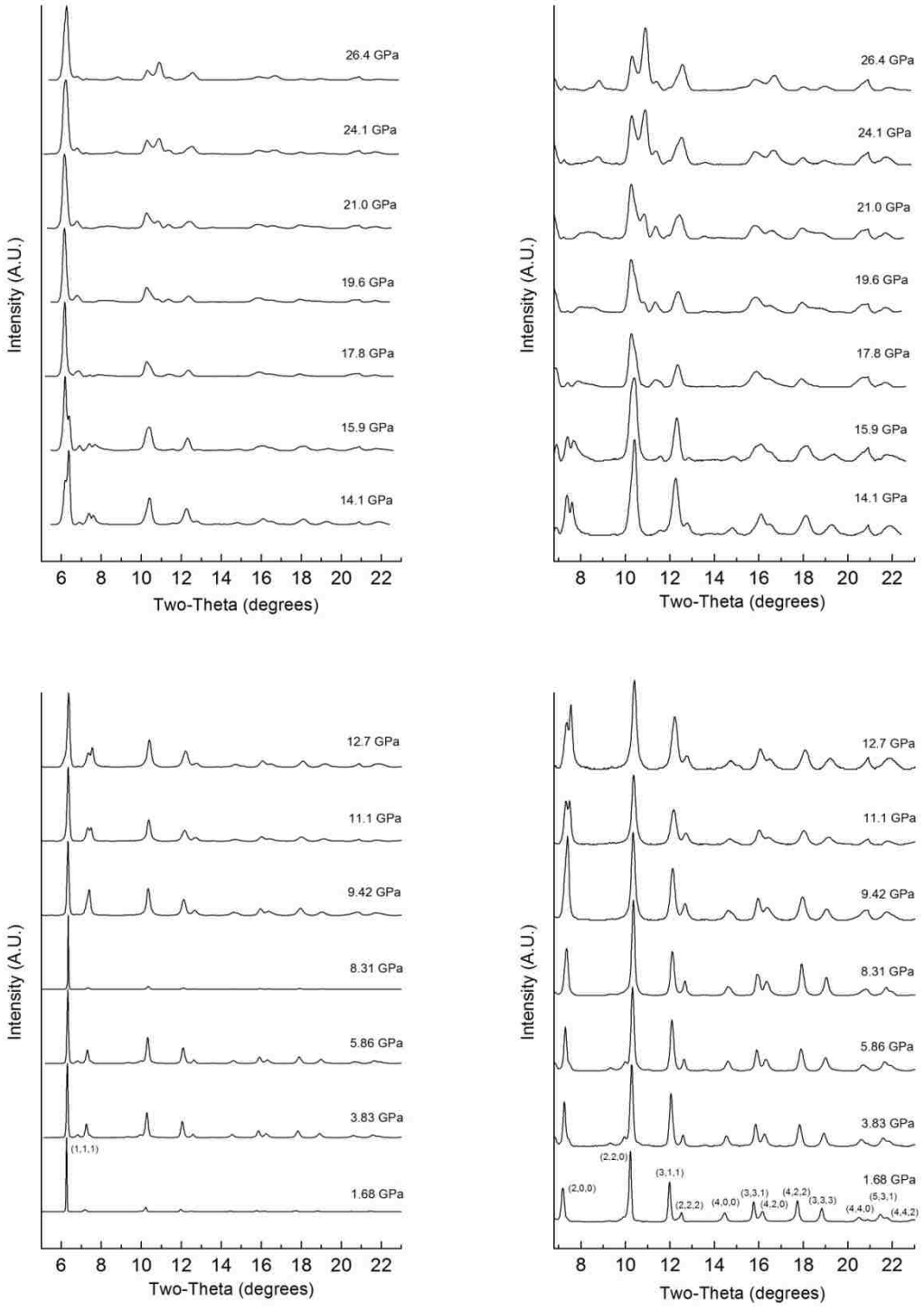

Figure 7. On the left, the evolution of XRD patterns for $AuAl_2$ up to 26.4 GPa is plotted over the full two-theta range and on the right, the same XRD patterns are plotted over a smaller range, from 7° to 23°, and are scaled to depict the lower intensity peaks more clearly at the higher two-theta angles. The hkl values are labeled for the lowest pressure point.

Fig. 9 has an EOS both for the low pressure phase and the high pressure phase as determined by Garg *et al*, the filled points being from the low pressure phase and the unfilled from the high pressure phase.

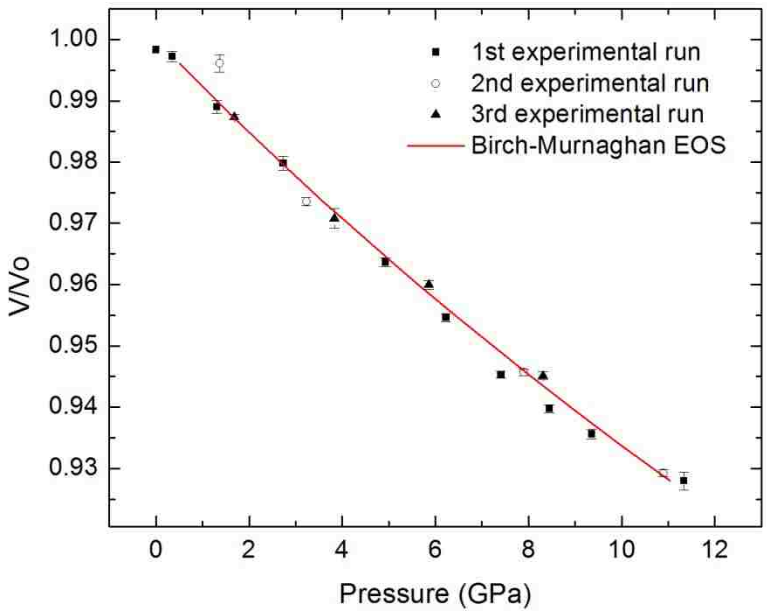

Figure 8. $AuAl_2$ volume and pressure data with Birch-Murnaghan EOS fit

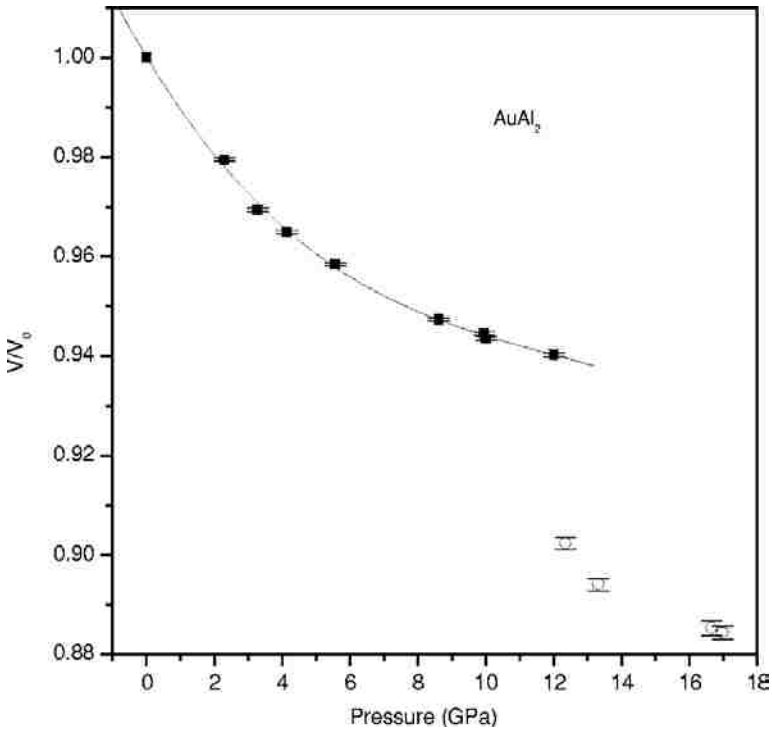

Figure 9. Garg *et* al, $AuAl_2$ volume versus pressure plot with fitted Birch-Murnaghan EOS [8]

Low Pressure Phase Results: $AuGa_2$

In **Fig. 10**, the XRD patterns for each pressure point are plotted for $AuGa_2$ to a maximum pressure of 20 GPa. The XRD patterns from 0.45 GPa to 7.89 GPa can be indexed to the ambient *Fm3m* phase. The patterns corresponding to 9.28 GPa and higher pressures are not able to be indexed to the same phase and as such, they are not used in the volume and pressure data for the Birch-Murnaghan EOS fit and will be discussed in a later section.

Using the same analysis procedure as was used for $AuAl_2$, the unit cell volume at each pressure point can be obtained from the XRD patterns for $AuGa_2$. This data, including the errors as calculated from the MDI Jade fitting, is contained in **Table 6**.

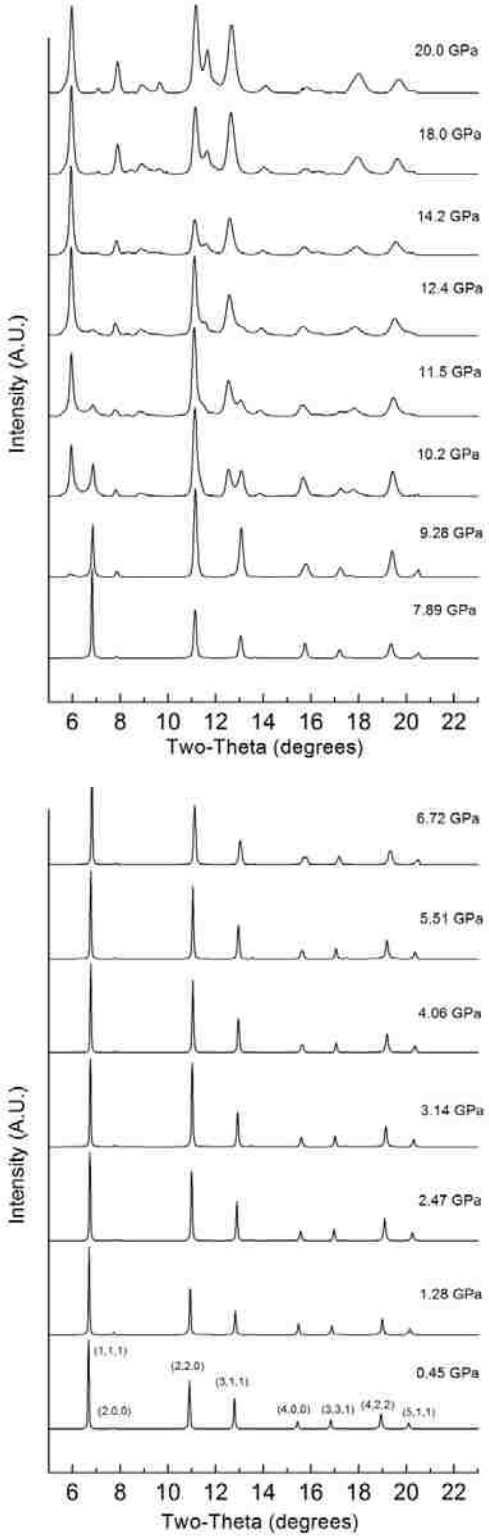

Figure 10. The evolution of XRD patterns for $AuGa_2$ up to 20.0 GPa. The hkl values are labeled for the lowest pressure point.

Pressure (GPa)	Volume (Å^3)	Error (Å^3)
0	224.76	
0.45	223.42	0.14
1.19	221.46	0.12
1.26	221.76	0.31
2.47	218.14	0.21
3.15	216.26	0.20
3.91	215.44	0.16
4.05	214.57	0.19
5.44	212.23	0.12
5.5	212.25	0.59
6.41	210.99	0.25
6.72	210.33	1.05
7.15	209.55	0.18

Table 6. Pressure and volume data for $AuGa_2$ from two experimental runs

Fig. 11 has this data plotted along with the Birch-Murnaghan EOS fit to the data. In **Fig. 12**, the pressure versus volume data from Garg is plotted for comparison. No EOS is shown on the plot, but as seen in **Table 5**, values for the parameters of an EOS were obtained. **Table 5** has the parameters of this fit listed as well as the literature values for comparison.

While the bulk modulus as determined from these experiments lies within the range of values as calculated theoretically, it is slightly lower than the bulk modulus listed in the literature as found experimentally, unlike the higher value obtained for $AuAl_2$. However, considering the error on the value as determined by the fitting routine, this value of 90 ± 3 GPa is fairly close to the 98 GPa as found in the literature. The value found for the initial unit cell volume in our experiments is slightly lower than found in Garg *et al* [10] as seen in the table, but again, lies within the calculated results as determined by Li *et al* [7]. $\mathbf{B_0'}$ was fixed at a value of four for our experiments and the

experiments done in literature. However, the values from the theoretical calculations are much higher than either set of experiments.

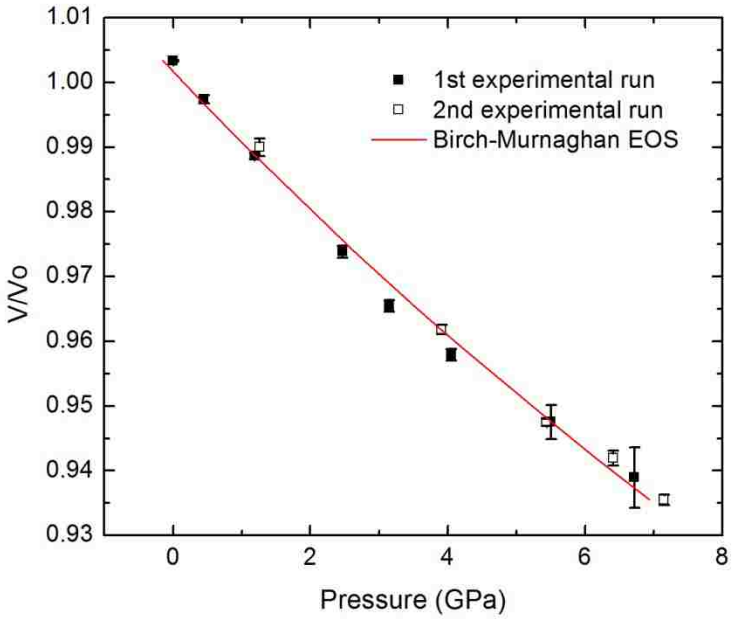

Figure 11. $AuGa_2$ volume and pressure data with Birch-Murnaghan EOS fit

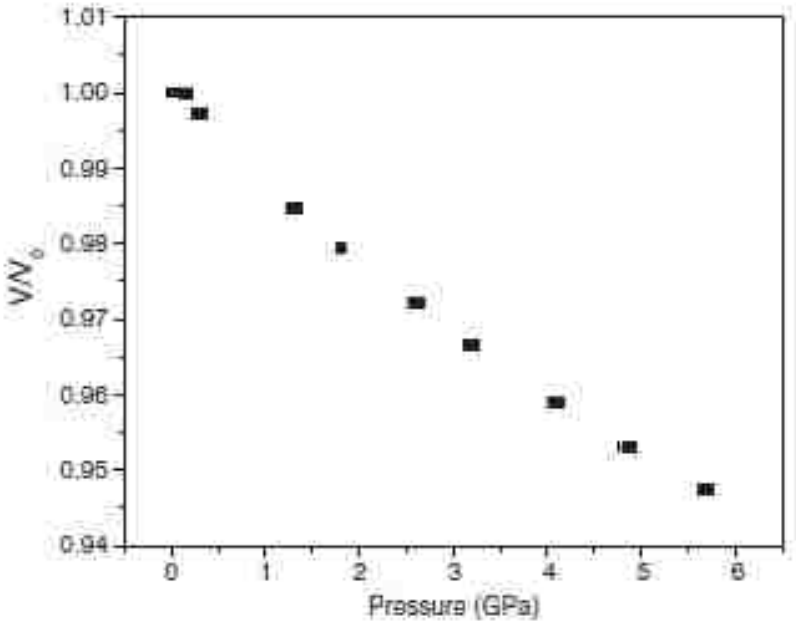

Figure 12. $AuGa_2$ volume versus pressure plot from Garg *et al*. [10]

Low Pressure Phase Results: $AuIn_2$

In **Fig. 13**, the XRD pattern for each pressure point is plotted for $AuIn_2$ to a maximal 21.3 GPa. As evidenced by the Figure, the XRD patterns are unchanged aside from the expected movement to higher two-theta angles until the pattern corresponding to 12.6 GPa. The XRD patterns up to 12.6 GPa can be indexed to the ambient structure CaF_2 (*Fm3m*) just as with $AuAl_2$ and $AuGa_2$. The higher pressure patterns cannot be indexed to the CaF_2 structure, and instead belong to a different phase. These patterns will be discussed in a later section.

For the patterns indexed to the CaF_2 phase, the same analysis procedure that was applied to $AuAl_2$ and $AuGa_2$ can be used. The volume and pressure data from applying this procedure is contained in **Table 7** along with the error as determined by the MDI Jade peak fitting. This data is plotted in **Fig. 14** along with the Birch-Murnaghan EOS fit to the data. The volume versus pressure plot and EOS fit from Godwal's work is shown in **Fig. 15** for comparison. The parameters for the fit are contained in **Table 5** as well as the literature values so as to compare the parameters.

The bulk modulus as obtained from this thesis' experiments for $AuIn_2$ agrees fairly well with the literature value as found experimentally. It is higher than the literature value, as $AuAl_2$'s bulk modulus was, but it is closer to the value than $AuAl_2$ had been. When compared to the values obtained using DFT calculations, the value lies well within the range of values calculated. Again, the initial volume is lower for this set of experiments when compared with the literature value in the table, as with all the samples, when the value is compared to the theoretically calculated value, it lies within the range of values from the different methods. An important difference between $AuIn_2$ and the

other samples studied in this thesis is the pressure derivative of the bulk modulus not being fixed to a value of four for $AuIn_2$. The curvature of the volume versus pressure data is too large for the typical value of four to account for it, and instead this larger $\mathbf{B_0'}$ is the value obtained from the fitting of the data.

Pressure (GPa)	Volume (Å^3)	Error (Å^3)
0	276.02	
0.64	273.46	0.06
1.33	271.22	0.03
2.31	267.87	0.20
2.39	267.55	0.06
2.93	265.94	0.01
3.29	264.54	0.06
3.67	262.85	0.12
4.82	259.86	0.12
5.27	259.24	0.05
5.39	258.92	0.07
6.19	256.78	0.17
7.15	255.19	0.07
7.73	253.91	0.06
8.02	253.64	0.11
8.81	252.02	0.07
9.54	250.54	0.19
9.56	250.92	0.05
9.85	250.28	0.10
11.01	249.73	0.18
11.04	248.54	1.13

Table 7. Pressure and volume data for $AuIn_2$ from two experimental runs

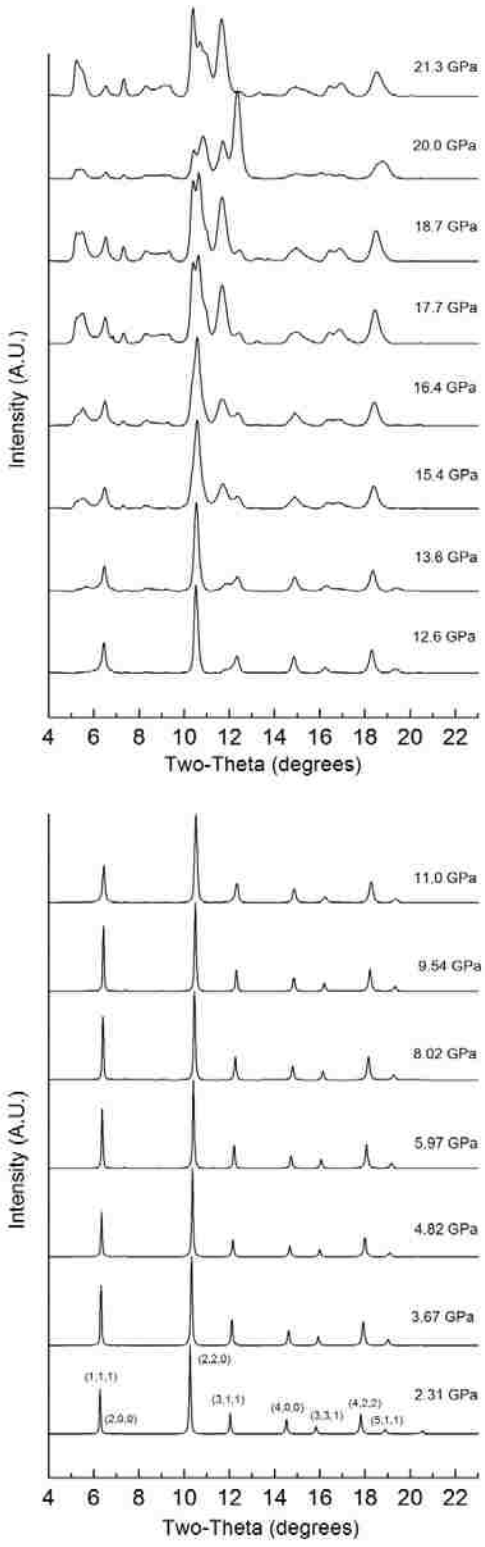

Figure 13. The evolution of XRD patterns for $AuIn_2$ up to 21.3 GPa. The hkl values are labeled for the lowest pressure point.

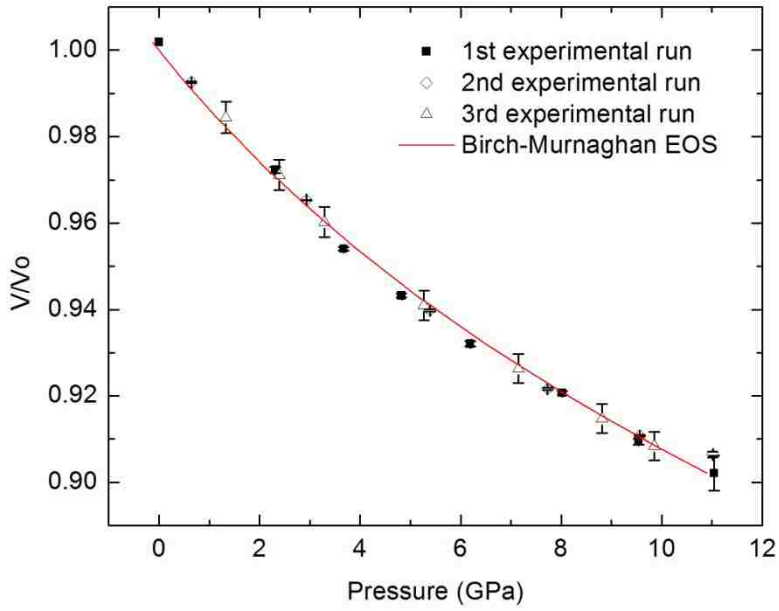

Figure 14. $AuIn_2$ volume and pressure data with Birch-Murnaghan EOS fit

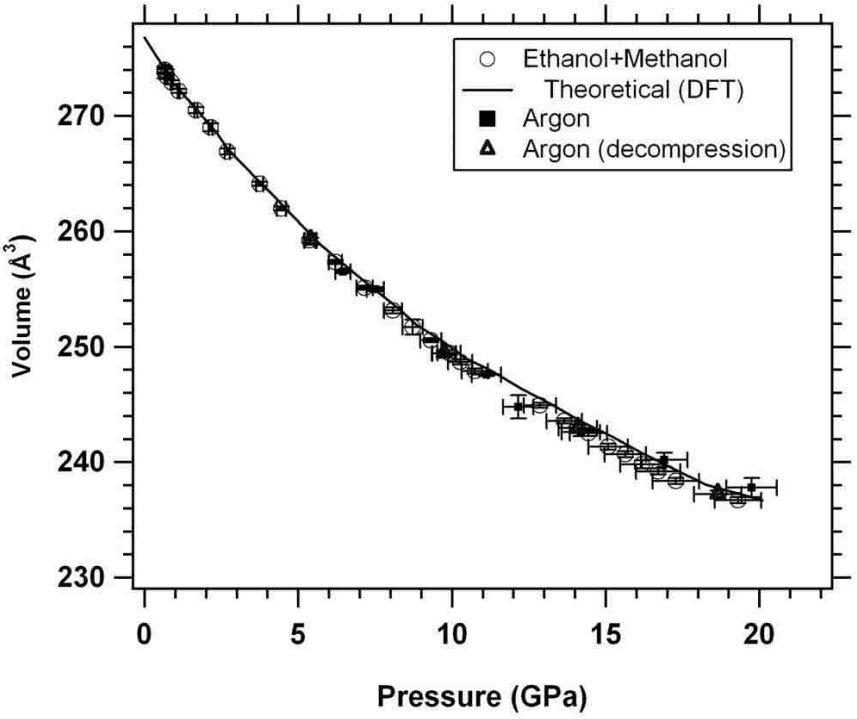

Figure 15. Godwal *et* al, $AuIn_2$ volume versus pressure plot with fitted Birch-Murnaghan EOS [13]

High Pressure Phase Results: $AuAl_2$

The Garg *et al* results discussed earlier are depicted in a plot from their publication in **Fig. 17**. The beginning of the transition, as discussed in their work, is indicated by a splitting of the (1,1,1) peak between 12 and 13 GPa. [13] In this work, in the 12.7 GPa XRD pattern depicted in **Fig. 7**, the (1,1,1) peak has a shoulder that was not seen in the previous XRD pattern. However, a splitting in the (2,0,0) peak is seen in the same pressure region as Garg *et al* observed the splitting in the (1,1,1) peak, which still indicates the beginning of a pressure-induced phase transition at the same pressure as the literature work. The completion of the phase transition as indicated in the plot of Garg's in **Fig. 17** is 17.0 GPa, but from the data collected in this thesis, it seems this phase does not complete until much higher pressures as the XRD patterns continuously change well beyond 17 GPa in **Fig. 7**. Attempts at indexing the high pressure phase of $AuAl_2$ were made, but none were successful in identifying the space group to which the orthorhombic phase belongs. Garg *et al*. stated that there were too few peaks available at these higher pressures in order to determine the specific space group of this high pressure phase, and the same seems to be true with the data collected in the experiments discussed in this thesis.

However, as mentioned previously, theoretical work has been done which determined which phase $AuAl_2$ exists in at high-pressure. Using this information, the data obtained from this thesis was fit to the *Pnma* structure. The pressure versus volume plot shown in **Fig. 16** includes the data from the previous CaF_2 phase as well as the *Pnma* high-pressure phase. Because of fluctuations in the data as fitted, an accurate EOS is not able to be obtained for the *Pnma* phase. But, information can still be obtained regarding

the phase transition from the pressure versus volume data in **Table 8**. The volume before the transition as found in **Table 4** was 200.28 ± 0.31 Å and after the transition at 14.1 GPa in **Table 8** the volume was found to be 190.84 ± 0.89 Å, which gives a percentage volume change of 4.7 % which compares reasonably with the 3 – 4 % volume change found by Garg *et al* when fitting it to a general orthorhombic cell. [8]

Pressure (GPa)	Volume ($Å^3$)	Error ($Å^3$)
14.1	190.84	0.89
15.7	188.71	0.81
17.9	187.29	1.37
19.6	186.71	1.06
21	185.15	1.40
23.8	182.09	1.19
26	181.87	1.55

Table 8. Volume versus pressure data for *Pnma* phase of $AuAl_2$

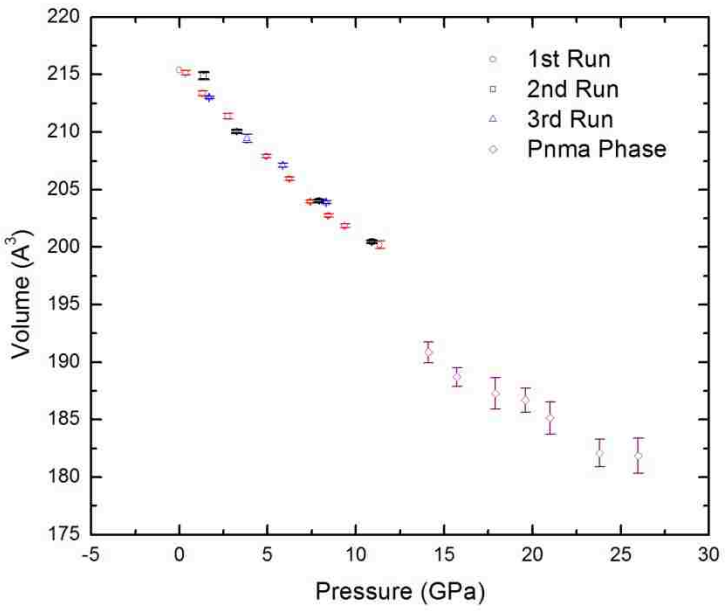

Figure 16. Volume versus pressure plot of low-pressure CaF_2 phase and high-pressure *Pnma* phase for $AuAl_2$.

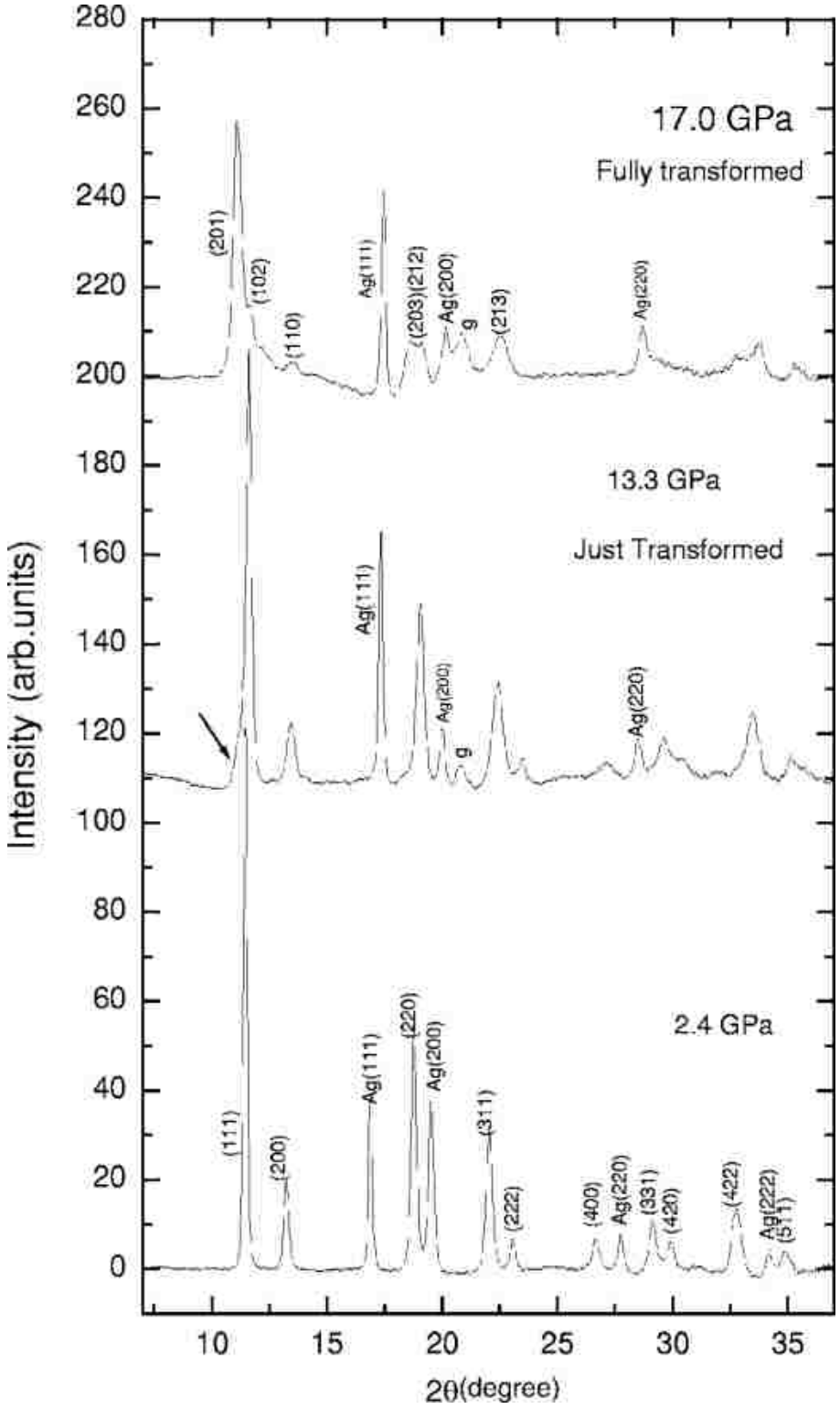

Figure 17. Evolution of XRD patterns for $AuAl_2$ from Garg et al. In the range of 2.4 GPa to 13.3 GPa the structure remains CaF_2 but at 13.3 GPa a change in the XRD patterns is seen and is indicative of a pressure-induced phase transition which completes at 17.0 GPa

High-Pressure Phase Results for $AuGa_2$

Looking at the XRD patterns in **Fig. 10**, the first evidence of a change in the patterns is in the 9.28 GPa, which suggests the beginning of a phase transition. Several peaks both appear and disappear constantly as the pressure is increased. The (1,1,1) peak slowly disappears from the 9.28 GPa pattern to the 14.2 GPa pattern. In this same pressure range, the (3,1,1) peak splits and the new peak becomes prominent while the original peak vanishes completely at the highest pressures. Another important feature is the (2,2,0) peak begins to have a shoulder peak at 10.2 GPa that continues to increase in intensity while the original (2,2,0) peak decreases slightly but remains a prominent feature throughout the entire pressure range depicted in **Fig. 10**. Other peaks split as well as appear and disappear throughout this pressure range suggesting that $AuGa_2$ does not transform directly into a particular phase and instead has a constantly changing mixed phase over this pressure range.

In Garg *et al*, as mentioned previously, $AuGa_2$ is reported to undergo a phase transition after 7 GPa. [10] This is slightly lower than the onset of a phase transition as seen in $AuGa_2$ in this study. In the Garg study, the XRD patterns between 7 GPa and 10 GPa were able to be fitted to a low symmetry orthorhombic phase, but the patterns at pressures higher than 10 GPa were unable to be fit because they continuously changed. The continual changing in the XRD patterns was observed in the experimental data for $AuGa_2$ from this study, but none of the XRD patterns would fit to any orthorhombic phase.

High-Pressure Phase Results for $AuIn_2$

As can be seen in the XRD patterns in **Fig. 13**, new diffraction peaks begin to appear in the pattern corresponding to 12.6 GPa. The first of these new peaks noticed in the XRD patterns is a small peak appearing next to the (3,1,1) peak. As the pressure increases further, more new peaks begin to emerge, but what is important to note is that many of the peaks directly corresponding to the low pressure phase never disappear completely suggesting a mixed phase throughout all the XRD patterns up to 21.3 GPa. As mentioned previously, Godwal determined that a phase transition occurred in this material at 8 to 9 GPa and had completed by 17.4 GPa. [12] A plot of the XRD patterns as obtained by Godwal for $AuIn_2$ is shown in **Fig. 18**.

In **Fig. 18**, it is clear that a transition occurs between 9 GPa and 17.4 GPa GPa and the onset pressure is stated to be after the 9 GPa XRD pattern shown and completion of the phase transition is seen at 17.4 GPa. It was indexed by Godwal to a monoclinic phase. [12] In this particular study, the high-pressure phase was unable to be indexed to any phase, but there is very strong evidence from the XRD patterns that a phase transition is occurring.

Both the results from the experiments carried out for this thesis, and Godwal's 2002 results are in disagreement with a later Godwal publication, which was mentioned previously as well, where $AuIn_2$ is found to remain in the CaF_2 phase until 24 GPa and then at higher pressures, become amorphous. [13] Godwal mentions that non-hydrostatic conditions within the sample chamber of the DAC in the previous work may have caused a phase transition to occur. The PTM in the earlier study had been ethanol as compared to Ar gas in the 2008 study. Since the ethanol PTM used in the earlier Godwal study is

similar to the PTM used in our experiments, the appearance of the phase transition in both of these experiments may be dependent on the PTM used. Both ethanol and methanol:ethanol PTMs have a tendency to become non-hydrostatic at higher pressures and as such, non-hydrostatic conditions may play a role in the phase transition seen in $AuIn_2$.

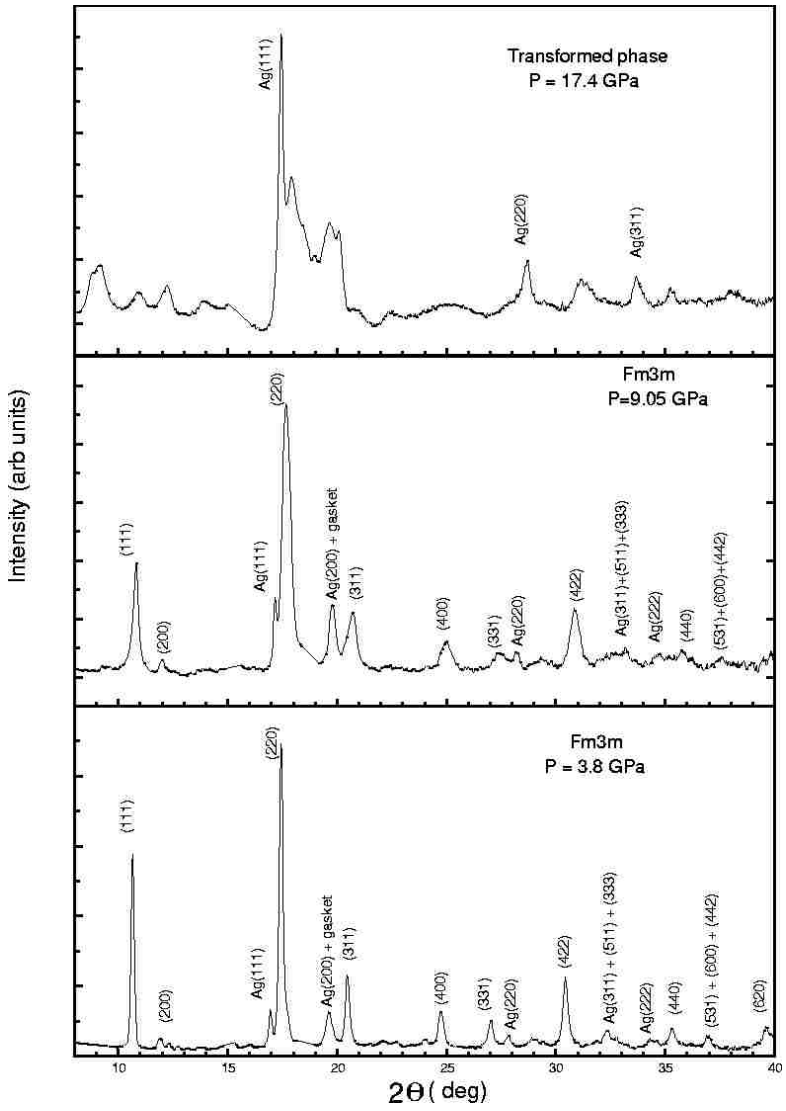

Figure 18. Evolution of XRD patterns for $AuIn_2$ as found experimentally by Godwal *et al*. [12]

Conclusions

This section will give a brief overview of the results as found in this series of experiments as well as potential future experiments and analysis that can be done to develop the results on these three compounds further.

$AuAl_2$

A volume versus pressure plot was obtained for both the lower pressure phase, below 13 GPa, and the higher pressure phase, above 13 GPa but a valid EOS was only obtained for the lower pressure phase. The lower pressure phase was fit to the phase as determined at ambient pressure conditions, which was the CaF_2 type *Fm3m* cubic phase, which agrees with the literature. From this EOS, the bulk modulus of $AuAl_2$ is found to be the largest, and as such, it is the least compressible of the three intermetallic compounds.

The higher pressure phase was fit to the *Pnma* orthorhombic phase in agreement with the theoretical results as found by Verma *et al*. The onset and completion of the pressure induced structural phase transition for $AuAl_2$ reported in the literature varies from our experiment. The onset of the transition in the literature is 13.3 GPa and in our experiment it occurs as early as 11 GPa. The completion of the transition as determined by Garg *et al* was approximately 17 GPa, but in this experiment, the phase transition seems more sluggish and does not complete throughout the pressure range studied. The discrepancies in the onset and completion pressures for the phase transitions is possibly caused by differing experimental conditions inside the DACs. The effect of pressure

transmitting media and non-hydrostaticity also play an important role in changing the onset and completion of the transition, which needs to be studied further.

$AuGa_2$

$AuGa_2$ stays in the CaF_2 type *Fm3m* cubic phase from ambient pressure to 9.28 GPa. At higher pressures, the XRD patterns show additional peaks which continuously evolve throughout the entire range of pressures studied in this experiment, which makes identification of high pressure phase difficult. Below this pressure, the volume versus pressure plot and EOS were obtained for $AuGa_2$. From the value of the bulk modulus as obtained from determining the EOS, it is seen that $AuGa_2$ has a value lower than that of $AuAl_2$ but larger than $AuIn_2$ making it less compressible than $AuIn_2$, but more compressible than $AuAl_2$.

The new peaks appearing at 9.28 GPa are strong evidence for a structural phase transition occurring in this material, but this pressure for the onset of the transition is at a higher value than previously reported by Garg *et al*, where the transition was observed to begin at 7 GPa. This difference in the onset pressure of the pressure-induced structural phase transition is likely due to differing conditions inside the DAC used in our experiments compared to the DAC used in Garg's study. Garg *et al* was able to fit the XRD patterns between 7 and 10 GPa to a low symmetry orthorhombic phase, but even in this region, the data from the current experiment could not be fit to any phase and leaves room for further investigation.

$AuIn_2$

Up to 12.6 GPa, $AuIn_2$ remains in the ambient pressure CaF_2 type *Fm3m* phase. After this pressure, there is definite evidence of a pressure induced phase transition observed due to emergence of new additional peaks, but the XRD patterns were not indexed to any particular phase due to sluggish phase change up to the maximum pressure achieved in the experiment. An EOS for the low pressure CaF_2 phase was obtained for $AuIn_2$, but because of the inability to fit the high pressure patterns, there is no volume versus pressure plot or EOS for the higher pressure phase. From the parameters of this EOS fitted to the experimental data, $AuIn_2$ is determined to be the most compressible of the three intermetallic compounds with a bulk modulus of 68 ± 2 GPa as compared to $AuAl_2$'s bulk modulus which is 122 ± 2 GPa.

The onset of this phase transition, 12.6 GPa, is higher than the previously reported phase transition for this material by Godwal *et al*, 9 GPa. In Godwal's work, the phase was indexed as a monoclinic phase which completed its transformation at 17.4 GPa. Despite the difference in onset and completion pressure for the phase transition, the evidence of a phase transition agrees with Godwal's work. Both of these works are in disagreement with Godwal's 2008 paper, which reports no evidence of a phase transition in $AuIn_2$ all the way to 24 GPa. An explanation given for the difference between the two works of Godwal's is non-hydrostatic conditions inside the sample chamber of the DAC as liquid PTM was used as compared to gaseous PTM used in the later work. Since both studies with liquid PTM show evidence of a phase transition and these liquid PTMs have a tendency to be more non-hydrostatic than gaseous PTMs, it is possible the transition is

induced by non-hydrostatic conditions. Extending the pressure range and understanding the effect of PMT are under progress.

References

[1] Mansour, A. N., Dmitrienko A., and Soldatov, A. V., Physical Review B **55** (1997)
[2] Matthias, B.T., Geballe, T. H., Geller, S., and Corenzwit, E. Physics Review **95** (1954)
[3] E. Hahn and B. O. Seraphin, Phys. Thin Films **10**,1 (1978).
[4] Bosch W P, Chinchure A, Flokstra J, de Groot M J, Van Heumen E, Jochemsen R, Mathu F, Peruzzi A and Veldhuis D http://www.xs4all.nl/~hdleiden/srd1000/reports/srd1000.doc
[5] S. Rehmann, T. Herrmannsdorfer, and F. Pobell, Phys. Rev. Lett. **78**, 1122 (1997).
[6] Lince J R and Williams R S 1985 *J. Vac. Sci. Technol.* A **3** 1217
Lince J R and Williams R S 1986 *Thin Solid Films* **137** 251
[7] Li, Q., et al. J. Phys.: Condens. Matter **19** (2007) 425224 (13pp)
[8] Garg AB., et al. Physical Review B **72**, 024112 (2005)
[9] Verma, A. K., Modak, P., Sharma, S. M., J. Phys.: Condens. Matter **20** (2008)
[10] Garg A.B., et al. J. Phys.: Condens. Matter **18** 8523–8532 (2006)
[11] Godwal, BK., et al. Physical Review B **57** (1998)
[12] Godwal, BK., et al. Physical Review B, **65**, 140101 (2002)
[13] Godwal, BK., et al. Physical Review B **78**, 094107(2008)
[14] http://stwww.weizmann.ac.il/lasers/laserweb/Ch-6/C6s2t1p2.htm
[15] http://www.geo.arizona.edu/xtal//group/images/ruby_fluorescence.JPG
[16] Mao, HK., *et al.* J. Appl.Phys. **49**, 3276 (1978)
[17] Kittel, Charles. *Introduction to Solid State Physics.* 8th ed.
[18] F. Birch, J. Appl. Phys. **9**, 279 (1938)
[19] Materials Data Incorporated, 1224 Concannon Blvd., Livermore, California 94550, USA.
[20] A. P. Hammersley, S. O. Svensson, M. Hanfland, A. N. Fitch, and D. Haüsermann, High Press. Res. **14**, 235 (1996).

Vita

The Graduate College
University of Nevada, Las Vegas

Jason Baker

Degrees:

Bachelor of Science, Physics, 2008
University of Nevada, Las Vegas

Publications:

Ravhi S. Kumar, Yi Zhang, Yuming Xiao, **Jason Baker**, Andrew Cornelius, Sathishkumar Veeramalai, Paul Chow, Changfeng Chen, Yusheng Zhao. APL **99**, 000000 (2011)

Jason Baker, Ravhi Kumar, Andrew Cornelius. *High Pressure Structural Studies of AuX_2 (X = Al, Ga, In).* Stewardship Science Academic Alliance Symposium. Poster. (2010)

Jason Baker, Ravhi Kumar, Andrew Cornelius. *High Pressure X-Ray Diffraction of $AuAl_2$.* HiPSEC Annual Review. Poster. (2009)

Thesis Title:

Synthesis and High-Pressure Structural Studies of AuX_2 (X = Al, Ga, In) Compounds

Thesis Committee

Committee Chair: Dr. Andrew Cornelius
Committee Co-Chair: Dr. Ravhi Kumar
Committee Member: Dr. Changfeng Chen
Committee Member: Dr. Michael Pravica
Graduate Faculty Representative: Dr. Clemens Heske